

XRISM/Resolve View of Abell 2319: Turbulence, Sloshing, and ICM Dynamics

XRISM COLLABORATION, Marc AUDARD,¹ Hisamitsu AWAKI,² Ralf BALLHAUSEN,^{3,4,5} Aya BAMBA,⁶ Ehud BEHAR,⁷ Rozenn BOISSAY-MALAUQUIN,^{8,4,5} Laura BRENNEMAN,⁹ Gregory V. BROWN,¹⁰ Lia CORRALES,¹¹ Elisa COSTANTINI,¹² Renata CUMBEE,⁴ Maria DIAZ TRIGO,¹³ Chris DONE,¹⁴ Tadayasu DOTANI,¹⁵ Ken EBISAWA,¹⁵ Megan E. ECKART,¹⁰ Dominique ECKERT,¹ Satoshi EGUCHI,¹⁶ Teruaki ENOTO,¹⁷ Yuichiro EZOE,¹⁸ Adam FOSTER,⁹ Ryuichi FUJIMOTO,¹⁵ Yutaka FUJITA,¹⁸ Yasushi FUKAZAWA,¹⁹ Kotaro FUKUSHIMA,¹⁵ Akihiro FURUZAWA,²⁰ Luigi GALLO,²¹ Javier GARCÍA,^{4,22} Liyi GU,¹² Matteo GUAINAZZI,²³ Kouichi HAGINO,⁶ Kenji HAMAGUCHI,^{8,4,5} Isamu HATSUKADE,²⁴ Katsuhiko HAYASHI,¹⁵ Takayuki HAYASHI,^{8,4,5} Natalie HELL,¹⁰ Edmund HODGES-KLUCK,⁴ Ann HORNSCHMEIER,⁴ Yuto ICHINOHE,²⁵ Daiki ISHI,¹⁵ Manabu ISHIDA,¹⁵ Kumi ISHIKAWA,¹⁸ Yoshitaka ISHISAKI,¹⁸ Jelle KAASTRA,^{12,26} Timothy KALLMAN,⁴ Erin KARA,²⁷ Satoru KATSUDA,²⁸ Yoshiaki KANEMARU,¹⁵ Richard KELLEY,⁴ Caroline KILBOURNE,⁴ Shunji KITAMOTO,²⁹ Shogo B.KOBAYASHI,³⁰ Takayoshi KOHMURA,³¹ Aya KUBOTA,³² Maurice LEUTENEGGER,⁴ Michael LOEWENSTEIN,^{3,4,5} Yoshitomo MAEDA,¹⁵ Maxim MARKEVITCH,⁴ Hironori MATSUMOTO,³³ Kyoko MATSUSHITA,³⁰ Dan MCCAMMON,³⁴ Brian MCNAMARA,³⁵ Francois MERNIER,^{3,4,5} Eric MILLER,²⁷ Jon MILLER,¹¹ Ikuyuki MITSUISHI,³⁶ Misaki MIZUMOTO,³⁷ Tsunefumi MIZUNO,³⁸ Koji MORI,²⁴ Koji MUKAI,^{8,4,5} Hiroshi MURAKAMI,³⁹ Richard MUSHOTZKY,³ Hiroshi NAKAJIMA,⁴⁰ Kazuhiro NAKAZAWA,^{36,*} Jan-Uwe NESS,⁴¹ Kumiko NOBUKAWA,⁴² Masayoshi NOBUKAWA,⁴³ Hirofumi NODA,⁴⁴ Hirokazu ODAKA,³³ Shoji OGAWA,¹⁵ Anna OGORZALEK,^{3,4,5} Takashi OKAJIMA,⁴ Naomi OTA,⁴⁵ Stephane PALTANI,¹ Robert PETRE,⁴ Paul PLUCINSKY,⁹ Frederick PORTER,^{4,*} Katja POTTSCHMIDT,^{8,4,5} Kosuke SATO,⁴⁶ Toshiki SATO,⁴⁷ Makoto SAWADA,²⁹ Hiromi SETA,¹⁸ Megumi SHIDATSU,² Aurora SIMIONESCU,¹² Randall SMITH,⁹ Hiromasa SUZUKI,²⁴ Andrew SZYMKOWIAK,⁴⁸ Hiromitsu TAKAHASHI,¹⁹ Mai TAKEO,⁴⁹ Toru TAMAGAWA,²⁵ Keisuke TAMURA,^{8,4,5} Takaaki TANAKA,⁵⁰ Atsushi TANIMOTO,⁵¹ Makoto TASHIRO,^{28,15} Yukikatsu TERADA,^{28,15} Yuichi TERASHIMA,² Yohko TSUBOI,⁵² Masahiro TSUJIMOTO,¹⁵ Hiroshi TSUNEMI,³³ Takeshi TSURU,¹⁷ Hiroyuki UCHIDA,¹⁷ Nagomi UCHIDA,¹⁵ Yuusuke UCHIDA,^{31,*} Hideki UCHIYAMA,⁵³ Yoshihiro UEDA,⁵⁴ Shinichiro UNO,⁵⁵ Jacco VINK,^{56,12} Shin WATANABE,¹⁵ Brian J. WILLIAMS,⁴ Satoshi YAMADA,⁵⁷ Shinya YAMADA,²⁹ Hiroya YAMAGUCHI,¹⁵ Kazutaka YAMAOKA,³⁶ Noriko YAMASAKI,¹⁵ Makoto YAMAUCHI,²⁴ Shigeo YAMAUCHI,⁵⁸ Tahir YAQOUB,^{8,4,5} Tomokage YONEYAMA,⁵² Tessei YOSHIDA,¹⁵ Mihoko YUKITA,^{59,4} Irina ZHURAVLEVA,⁶⁰ Riccardo SEPPI,¹ Itsuki AIHARA,³⁰ and Yuki OMIYA^{36,*}

¹Department of Astronomy, University of Geneva, Versoix CH-1290, Switzerland

²Department of Physics, Ehime University, Ehime 790-8577, Japan

³Department of Astronomy, University of Maryland, College Park, MD 20742, USA

⁴NASA / Goddard Space Flight Center, Greenbelt, MD 20771, USA

⁵Center for Research and Exploration in Space Science and Technology, NASA / GSFC (CRESST II), Greenbelt, MD 20771, USA

⁶Department of Physics, University of Tokyo, Tokyo 113-0033, Japan

⁷Department of Physics, Technion, Technion City, Haifa 3200003, Israel

⁸Center for Space Sciences and Technology, University of Maryland, Baltimore County (UMBC), Baltimore, MD, 21250 USA

⁹Center for Astrophysics | Harvard-Smithsonian, Cambridge, MA 02138, USA

¹⁰Lawrence Livermore National Laboratory, Livermore, CA 94550, USA

- ¹¹Department of Astronomy, University of Michigan, Ann Arbor, MI 48109, USA
- ¹²SRON Netherlands Institute for Space Research, Leiden, The Netherlands
- ¹³ESO, Karl-Schwarzschild-Strasse 2, 85748, Garching bei München, Germany
- ¹⁴Centre for Extragalactic Astronomy, Department of Physics, University of Durham, Durham DH1 3LE, UK
- ¹⁵Institute of Space and Astronautical Science (ISAS), Japan Aerospace Exploration Agency (JAXA), Kanagawa 252-5210, Japan
- ¹⁶Department of Economics, Kumamoto Gakuen University, Kumamoto 862-8680 Japan
- ¹⁷Department of Physics, Kyoto University, Kyoto 603-8047, Japan
- ¹⁸Department of Physics, Tokyo Metropolitan University, Tokyo 192-0397, Japan
- ¹⁹Department of Physics, Hiroshima University, Hiroshima 739-8526, Japan
- ²⁰Department of Physics, Fujita Health University, Aichi 470-1192, Japan
- ²¹Department of Astronomy and Physics, Saint Mary's University, Nova Scotia B3H 3C3, Canada
- ²²California Institute of Technology, Pasadena, CA 91125, USA
- ²³European Space Agency (ESA), European Space Research and Technology Centre (ESTEC), 2200 AG Noordwijk, The Netherlands
- ²⁴Faculty of Engineering, University of Miyazaki, 1-1 Gakuen-Kibanadai-Nishi, Miyazaki, Miyazaki 889-2192, Japan
- ²⁵RIKEN Nishina Center, Saitama 351-0198, Japan
- ²⁶Leiden Observatory, University of Leiden, P.O. Box 9513, NL-2300 RA, Leiden, The Netherlands
- ²⁷Kavli Institute for Astrophysics and Space Research, Massachusetts Institute of Technology, MA 02139, USA
- ²⁸Department of Physics, Saitama University, Saitama 338-8570, Japan
- ²⁹Department of Physics, Rikkyo University, Tokyo 171-8501, Japan
- ³⁰Faculty of Physics, Tokyo University of Science, Tokyo 162-8601, Japan
- ³¹Faculty of Science and Technology, Tokyo University of Science, Chiba 278-8510, Japan
- ³²Department of Electronic Information Systems, Shibaura Institute of Technology, Saitama 337-8570, Japan
- ³³Department of Earth and Space Science, Osaka University, Osaka 560-0043, Japan
- ³⁴Department of Physics, University of Wisconsin, WI 53706, USA
- ³⁵Department of Physics & Astronomy, Waterloo Centre for Astrophysics, University of Waterloo, Ontario N2L 3G1, Canada
- ³⁶Graduate School of Science, Nagoya University, Aichi 464-8602, Japan
- ³⁷Science Research Education Unit, University of Teacher Education Fukuoka, Fukuoka 811-4192, Japan
- ³⁸Hiroshima Astrophysical Science Center, Hiroshima University, Hiroshima 739-8526, Japan
- ³⁹Department of Data Science, Tohoku Gakuin University, Miyagi 984-8588
- ⁴⁰College of Science and Engineering, Kanto Gakuin University, Kanagawa 236-8501, Japan
- ⁴¹European Space Agency (ESA), European Space Astronomy Centre (ESAC), E-28692 Madrid, Spain
- ⁴²Department of Science, Faculty of Science and Engineering, KINDAI University, Osaka 577-8502, JAPAN
- ⁴³Department of Teacher Training and School Education, Nara University of Education, Nara 630-8528, Japan
- ⁴⁴Astronomical Institute, Tohoku University, Miyagi 980-8578, Japan
- ⁴⁵Department of Physics, Nara Women's University, Nara 630-8506, Japan
- ⁴⁶Faculty of Science, Kyoto Sangyo University, Kyoto 603-8555, Japan
- ⁴⁷School of Science and Technology, Meiji University, Kanagawa, 214-8571, Japan
- ⁴⁸Yale Center for Astronomy and Astrophysics, Yale University, CT 06520-8121, USA
- ⁴⁹Faculty of Science, University of Toyama, Toyama 930-8555, Japan
- ⁵⁰Department of Physics, Konan University, Hyogo 658-8501, Japan
- ⁵¹Graduate School of Science and Engineering, Kagoshima University, Kagoshima, 890-8580, Japan
- ⁵²Department of Physics, Chuo University, Tokyo 112-8551, Japan
- ⁵³Faculty of Education, Shizuoka University, Shizuoka 422-8529, Japan
- ⁵⁴Department of Astronomy, Kyoto University, Kyoto 606-8502, Japan
- ⁵⁵Nihon Fukushi University, Shizuoka 422-8529, Japan
- ⁵⁶Anton Pannekoek Institute, the University of Amsterdam, Postbus 94249, 1090 GE Amsterdam, The Netherlands
- ⁵⁷RIKEN Cluster for Pioneering Research, Saitama 351-0198, Japan
- ⁵⁸Department of Physics, Faculty of Science, Nara Women's University, Nara 630-8506, Japan
- ⁵⁹Johns Hopkins University, MD 21218, USA
- ⁶⁰Department of Astronomy and Astrophysics, University of Chicago, Chicago, IL 60637, USA

*E-mail: omiya_y@u.phys.nagoya-u.ac.jp, nakazawa@u.phys.nagoya-u.ac.jp, yuuchida@rs.tus.ac.jp, frederick.s.porter@nasa.gov

ORCID: 0000-0002-1118-8470, 0000-0003-0890-4920, 0000-0001-9735-4873, 0000-0003-2704-599X, 0000-0003-2663-1954, 0000-0001-6338-9445, 0000-0002-5466-3817, 0000-0001-8470-749X, 0000-0001-9894-295X, 0000-0001-7796-4279, 0000-0002-1065-7239, 0000-0002-5352-7178, 0000-0003-3894-5889, 0000-0001-7917-3892, 0000-0003-2814-9336, 0000-0003-1244-3100, 0000-0003-3462-8886, 0000-0002-2374-7073, 0000-0003-0058-9719, 0000-0002-0921-8837, 0000-0001-8055-7113, 0009-0006-4968-7108, 0000-0003-3828-2448, 0000-0001-9911-7038, 0000-0002-1094-3147, 0000-0003-4235-5304, 0000-0001-7515-2779, 0000-0003-3518-3049, 0000-0001-6922-6583, 0000-0001-6665-2499, 0000-0003-3057-1536, 0000-0002-2397-206X, 0000-0001-8667-2681, 0000-0002-6102-1441, 0000-0001-5540-2822, 0000-0003-0172-0854, 0000-0002-1104-7205, 0000-0002-4541-1044, 0009-0007-2283-3336, 0000-0001-9464-4103, 0000-0001-8948-7983, 0000-0001-7773-9266, 0000-0002-3331-7595, 0000-0002-1661-4029, 0000-0002-9099-5755, 0000-0003-0144-4052, 0000-0003-2907-0902, 0000-0001-5170-4567, 0000-0002-7031-4772, 0000-0002-3031-2326, 0000-0003-2869-7682, 0000-0002-9901-233X, 0000-0003-2161-0361, 0000-0001-7263-0296, 0000-0002-0018-0369, 0000-0002-8286-8094, 0000-0002-7962-5446, 0000-0001-6988-3938, 0000-0003-2930-350X, 0000-0002-0726-7862, 0000-0003-1130-5363, 0000-0001-6020-517X, 0000-0002-5701-0811, 0000-0003-4504-2557, 0000-0002-6054-3432, 0000-0002-2784-3652, 0000-0002-8108-9179, 0000-0003-3850-2041, 0000-0003-1415-5823, 0000-0002-6374-1119, 0000-0002-4656-6881, 0000-0001-5774-1633, 0000-0003-2008-6887, 0000-0001-8195-6546, 0000-0002-9714-3862, 0000-0003-4284-4167, 0000-0002-8152-6172, 0000-0002-4974-687X, 0000-0001-6314-5897, 0000-0002-4383-0368, 0000-0002-0114-5581, 0000-0002-5097-1257, 0000-0002-2359-1857, 0000-0003-1780-5481, 0000-0002-9184-5556, 0000-0002-5504-4903, 0000-0003-1518-2188, 0000-0002-5641-745X, 0000-0002-7962-4136, 0000-0003-4580-4021, 0000-0001-7821-6715, 0000-0002-4708-4219, 0000-0003-0441-7404, 0000-0003-2063-381X, 0000-0002-9754-3081, 0000-0003-4808-893X, 0000-0002-5092-6085, 0000-0003-3841-0980, 0000-0003-4885-5537, 0000-0003-1100-1423, 0000-0001-6366-3459,

0000-0001-7630-8085, 0009-0009-9196-4174

Abstract

We present results from XRISM/Resolve observations of the core of the galaxy cluster Abell 2319, focusing on its kinematic properties. The intracluster medium (ICM) exhibits temperatures of approximately 8 keV across the core, with a prominent cold front and a high-temperature region (~ 11 keV) in the northwest. The average gas velocity in the $3 \text{ arcmin} \times 4 \text{ arcmin}$ region around the brightest cluster galaxy (BCG) covered by two Resolve pointings is consistent with that of the BCG to within 40 km s^{-1} and we found modest average velocity dispersion of $230\text{--}250 \text{ km s}^{-1}$. On the other hand, spatially-resolved spectroscopy reveals interesting variations. A blueshift of up to $\sim 230 \text{ km s}^{-1}$ is observed around the east edge of the cold front, where the gas with the lowest specific entropy is found. The region further south inside the cold front shows only a small velocity difference from the BCG; however, its velocity dispersion is enhanced to $\sim 400 \text{ km s}^{-1}$, implying the development of turbulence. These characteristics indicate that we are observing sloshing motion with some inclination angle following BCG and that gas phases with different specific entropy participate in sloshing with their own velocities, as expected from simulations. No significant evidence for a high-redshift ICM component associated with the subcluster Abell 2319B was found in the region covered by the current Resolve pointings. These results highlight the importance of sloshing and turbulence in shaping the internal structure of Abell 2319. Further deep observations are necessary to better understand the mixing and turbulent processes within the cluster.

Keywords: galaxies: clusters: individual (Abell 2319) – galaxies: clusters: intracluster medium – X-rays: galaxies: clusters – turbulence – large-scale structure of universe

1 Introduction

Massive galaxy clusters in the nearby universe, with intracluster medium (ICM) temperatures reaching approximately 10 keV, represent some of the largest gravitationally bound structures formed through the hierarchical growth of cosmic large-scale structure (e.g., Voit 2005; Kravtsov & Borgani 2012). These clusters often reside at the intersections of cosmic filaments, where frequent mergers occur, indicating ongoing mass assembly (e.g., Ricker & Sarazin 2001; Owers et al. 2011). Such mergers release tremendous gravitational energy, which is dissipated into the ICM via shocks and turbulence, resulting in substantial heating (e.g., Markevitch & Vikhlinin 2007; Shi et al. 2020; Okabe & Umetsu 2008). These processes also amplify magnetic fields and reaccelerate relativistic electrons, giving rise to diffuse synchrotron radio emission such as radio halos and relics (e.g., Feretti et al. 2012; Brunetti & Jones 2014; van Weeren et al. 2019). Understanding these mechanisms is crucial for quantifying the non-thermal energy content of clusters and the interplay between thermal and non-thermal components during structure formation. Although the spatial distribution and velocity dispersion of member galaxies provide constraints on merger geometries, high-resolution X-ray observations remain essential for probing the ICM and revealing features such as shock fronts, cold fronts, sloshing structures, and bulk motions (e.g., Markevitch & Vikhlinin 2007; Botteon et al. 2018). These observations offer key insights into the thermodynamical properties and the dynamical states of merging clusters (e.g., Yuan & Han 2020; Chadayammuri et al. 2022; Omiya et al. 2023).

Gravitational potential fluctuations, gas turbulence, and incomplete mixing of different entropy components during a cluster merger cause disturbances in the ICM across various scales (e.g., Paul et al. 2011; Mohapatra & Sharma 2019). These appear as surface brightness fluctuations and distortions in X-ray images, offering insights into merging structures (e.g., Churazov et al. 2012; Zhuravleva et al. 2018; Heinrich et al. 2024; Li et al. 2025). Although direct measurement of gas motion is limited by the resolution of X-ray CCDs, careful re-calibration of energy scales have enabled estimates of bulk ICM velocities to $\sim 200 \text{ km s}^{-1}$ level (Sanders et al. 2020; Omiya et al. 2024). The XRISM satellite (Tashiro et al. 2020), launched in 2023, can measure line-of-sight ICM velocities with $\sim 15 \text{ km s}^{-1}$ accuracy, offering a powerful tool for revealing merger geometry and internal ICM motion. These observations are crucial for understanding non-thermal energy production in the ICM (e.g., XRISM Collaboration et al. 2025a).

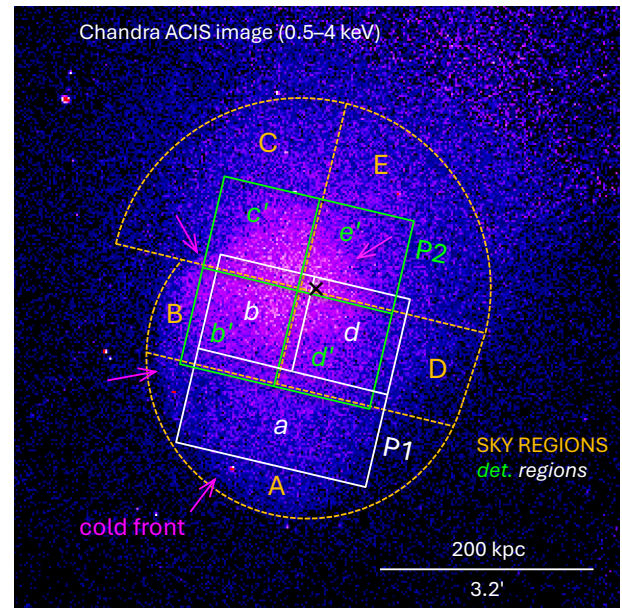


Fig. 1. Chandra image of A2319 in the 0.5–4.0 keV energy band (same as used in Wang 2019), overlaying regions used here for XRISM spatially-resolved spectroscopy. The boxes indicate the Resolve fields of view corresponding to observations P1 (white) and P2 (green), respectively. White boxes indicate the detector regions used for spectral extraction. For the P2 pointing, region names are labeled with a prime symbol (e.g., b', d') to distinguish them from those in P1. Note that Det-b and d in P1 are offset by approximately 0.5 pixel relative to Det-b' and d' in P2. The dashed orange regions represent the sky regions for which the ICM parameters are derived. A black "x" marks the position of the BCG, and purple arrows indicate the system of prominent cold fronts seen in the Chandra image. Alt text: Image of Abell 2319, with right ascension on the horizontal axis and declination on the vertical axis.

Abell 2319 (hereafter A2319) is one of the X-ray brightest nearby galaxy clusters ($z = 0.055$, Kluge & Bender 2023), characterized by a hot ICM with temperatures reaching ~ 8 keV and a prominent cold front near its center (e.g., Markevitch 1996; Molendi et al. 1999; Govoni et al. 2004; Ueda & Ichinohe 2024). Sunyaev-Zel'dovich effect measurements provide further evidence for the presence of hot gas in the outskirts, complementing the X-ray observations (Ghirardini et al. 2018; Hurier et al. 2019). Optical observations reveal that the brightest cluster galaxy (BCG), CGCG 230-007, has a redshift of $z_{\text{BCG}} = 0.05458$, which

matches that of the average redshift of the cluster (Oegerle et al. 1995). These observations also suggest that the system consists of two subclusters superimposed along the line of sight, A2319A and A2319B, indicating an ongoing merger. A giant radio halo extending to 2 Mpc further supports this scenario, although the detailed merger geometry remains under debate (Feretti et al. 1997; Govoni et al. 2001; Govoni et al. 2004; Million & Allen 2009; Farnsworth et al. 2013).

X-ray observations from Chandra reveal enhanced surface brightness extending counterclockwise from the BCG, suggestive of sloshing motions in the plane of the sky (Walker et al. 2016; Ichinohe et al. 2021). The radio halo shows a slight southwestward extension, possibly tracing turbulence induced by large-scale gas motions from southwest to northeast (Storm et al. 2015). In contrast, the redshift of the subcluster A2319B is offset by $\sim 3000 \text{ km s}^{-1}$ from the main cluster A2319A (Oegerle et al. 1995), implying a merger along the line of sight. These seemingly contradictory features raise the question of whether they originate from a single merger event or multiple distinct interactions.

A2319 was within the XRISM sky visibility window right after the launch. Consequently, the cluster was selected as one of the first-light observation targets of the mission (Uchida et al. 2025). In this study, we present results from XRISM/Resolve observations of the core of A2319, focusing on its thermodynamical properties and dynamical state. Throughout this paper, we use $H_0 = 70 \text{ km s}^{-1} \text{ Mpc}^{-1}$, $\Omega_m = 0.3$ flat cosmology, in which $1' = 62.3 \text{ kpc}$ at the cluster redshift. All errors are in 1σ confidence interval, otherwise noted.

2 Observations and Data Reduction

2.1 XRISM Observations

XRISM/Resolve conducted three observations of the central region A2319 between October 13 and 24, 2024. As shown in figure 1, two of these observations (OBSID: 000102000 and 000103000) were pointed near the cluster core (P2; RA, Dec = 290.298, 43.945) for 140 ks and 189 ks, respectively. The remaining observation (OBSID: 000101000) targeted a region near the cold front (P1; RA, Dec = 290.300, 43.924) for 147 ks. The three observations were carried out during the commissioning phase of the system. Because the gate valve opening operation did not go well, the original gain calibration plan cannot be used and the mission needed to establish the new gain calibration procedure. As such, a significant portion of the exposure time was conducted under the ^{55}Fe filter wheel configuration. As the Mn-K line emission and its tail were too strong, these data cannot be used for our study. The net exposure times with the open filter wheel configuration were approximately 49 ks, 89 ks, and 56 ks for OBSID 000102000, 000103000, and 000101000, respectively.

2.2 Data reduction and screening

To reconstruct the energy scale for the observation, we used a combination of the ^{55}Fe irradiation and, the calibration pixel to interpolate or extrapolate the detector gain of each pixel to the nearest filter wheel measurement. The observations of A2319 presented here were carried out very early in the XRISM commissioning phase, before the modern observing strategy was implemented. Thus the standard gain fiducial methodology was not employed, and specific treatment was applied. The detailed methodology is described in the Appendix 1.

We extracted spectra from a full array of 34 pixels, excluding pixel 27, which has exhibited aperiodic gain variations, and pixel 12, which is not within the field of view. For the event files, we applied DERIV_MAX-dependent RISE_TIME and STATUS[4] screening. In this analysis, we use only high-resolution primary (“Hp” or ITYPE = 0) events.

The response files were generated using HEASoft version 6.34. In creating the redistribution matrix file (RMF), we used cleaned event files to which the recommended additional screening had been applied and that included all grades except low-resolution secondary (Ls), to better reflect the Hp branching ratio. This exclusion was needed because of the large number of false Ls events associated with the on-board application of secondary-pulse detection to atypically shaped pulses such as clipped events. To better reproduce the detector response, the whichrmf option was set to “L”. The ancillary response file (ARF) was generated using xarfgen with the Chandra image as the input X-ray surface brightness distribution. A non-X-ray background (NXB) spectrum was extracted from a NXB database (v2) of Resolve night-Earth data using rslnxbgen and weighting by the distribution of geomagnetic cutoff rigidity sampled during each observation.

3 Data Analysis and Results

3.1 Spectral modeling

Spectral fitting to the Resolve data was done using XSPEC version 12.12.0 (Arnaud 1996), adopting the atomic database AtomDB version 3.0.9 for plasma model calculations. All elemental abundances are given relative to the protosolar values reported by Lodders et al. (2009). To model the emission from the ICM, we employed the velocity-broadened, collisional ionization equilibrium model (*bapec*) (Smith et al. 2001) in XSPEC. This model allows the plasma temperature, elemental abundances, redshift, and velocity broadening to be treated as free parameters. Thermal broadening is also included. Although correction to satellite’s orbital motion was not applied, to enable comparison with galaxy velocities measured in the optical band, we applied an average heliocentric correction to the fitted redshift by subtracting 12.42 km s^{-1} , calculated using the barycen tool in HEASoft. For the Galactic absorption, we used the multiplicative absorption model (*tbabs*), fixing the hydrogen column density to $11.2 \times 10^{20} \text{ cm}^{-2}$, as determined by Willingale et al. (2013). The NXB spectra of Resolve were modeled with a combination of power-law continuums and Gaussian lines, and incorporated into the spectral fitting as an additive background components. The cosmic X-ray background was not considered, as it is less than 1% of the celestial signal anywhere in the 3–9.5 keV energy band. Model fitting was evaluated using the C-statistic (Cash 1979).

3.2 Spectral fitting of full array

We performed spectral fitting of the full-array Resolve data from observations P1 and P2. Both 000102000 and 000103000 observed the same region P2, and its difference is negligible. We therefore linked the parameters between them.

It has been previously reported that the effective area calibration of Resolve is subject to significant uncertainties at low energy. To mitigate this issue, we limited the fitting energy range to 3.0–9.5 keV in this analysis.

The best-fit model parameters of the single-component fitting are listed in table 1, and the spectra with the best-fit model are

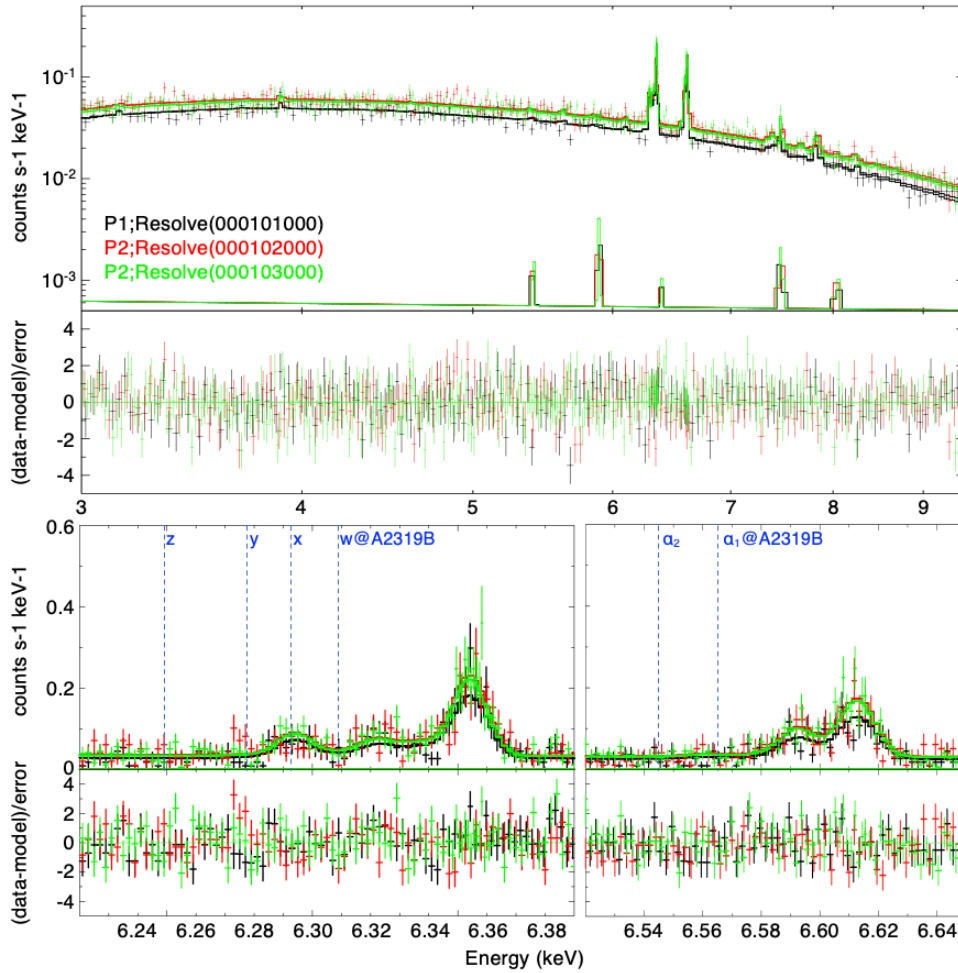


Fig. 2. (Top) Resolve spectra in the 3.0–9.5 keV energy band for regions P1 and P2. The spectra shown in black, red, and green represent Resolve observational data corresponding to OBSIDs 000101000, 000102000, and 000103000, respectively. The best-fit models are overlaid on each spectrum with NXB models, illustrating the goodness of fit between the observational data and the corresponding model. Data are binned by a factor of 4 eV for display purposes. (Bottom) Zoom-in of the Resolve spectra around the He-like Fe lines (left) and H-like Fe lines (right). Data are binned by a factor of 2 eV for display purposes. The blue lines indicate the expected line centers of He-like Fe $K\alpha$ complex (w, x, y, z) and H-like Fe $Ly_{\alpha 1,2}$ with a velocity of 18636 km s^{-1} , which is an average velocity of A2319B. Alt text: Three line graphs. In the upper panel, the x axis shows the energy from 3.0 to 9.5 kilo electron volt. The y axis shows the count from 0.0005 to 0.5 counts per second and per kilo electron volt, and the residuals of minus 5 to 5 in lower part. In the lower left panel, the x axis shows the energy from 6.22 to 6.40 kilo electron volt. In the lower right panel, the x axis shows the energy from 6.50 to 6.68 kilo electron volt. The y axis shows the count from 0.0 to 0.6 counts per second and per kilo electron volt, and the residuals of minus 5 to 5 in lower part.

Table 1. Best-fit Parameters of full array in 3.0–9.5 keV energy range.

Parameter	P1	P2
kT (keV)	$8.88^{+0.32}_{-0.33}$	$9.48^{+0.20}_{-0.20}$
Abundance (Z_{\odot})*	$0.42^{+0.03}_{-0.03}$	$0.44^{+0.02}_{-0.02}$
Redshift ($\times 10^{-2}$)	$5.4466^{+0.0079}_{-0.0099}$	$5.4490^{+0.0048}_{-0.0053}$
Relative Velocity (km s^{-1}) [†]	-37^{+30}_{-24}	-30^{+16}_{-14}
Velocity dispersion (km s^{-1})	249^{+24}_{-23}	232^{+14}_{-14}
C-stat/d.o.f	13367/12994	27972/25992

*: We adopted the solar abundance table of Lodders et al. (2009).

[†]: Velocity relative to BCG.

shown in figure 2. Overall, the bulk ICM velocity agrees well with that of the BCG, typically within $\sim 40 \text{ km s}^{-1}$. The ICM velocity dispersion is measured to be about $230\text{--}250 \text{ km s}^{-1}$, which

is comparable to that at the center of the Coma cluster (XRISM Collaboration et al. 2025b). Although the velocity dispersions are similar among the two clusters, the effective length scales over which they are measured are smaller in A2319 due to the presence of a denser core. Based on deprojected density and temperature profiles, we roughly estimate the effective length to be $150\text{--}200 \text{ kpc}$ in P1 and P2 of A2319, compared to $\sim 250 \text{ kpc}$ in the core pointing of the Coma cluster. This difference implies a more dynamically disturbed state in P1 and P2 of A2319.

Furthermore, a recent study using surface brightness fluctuation techniques with Chandra data reports an ICM velocity of $\sim 250 \text{ km s}^{-1}$ within R_{2500} ($\sim 700 \text{ kpc}$) for A2319 (Heinrich et al. 2024). Although the analyzed region and methodology differ from our XRISM-based approach, the derived velocity scale is in overall agreement with our results. Notably, the fluctuation-based method captures a broad range of velocity modes across spatial scales from a few tens to several hundred kiloparsecs, reinforcing the physical

consistency between these independent diagnostics of the ICM velocity field.

3.3 Spatially resolved spectroscopy

To quantitatively investigate the spatial structure of the ICM, we performed a spatial-spectral mixing (SSM) analysis. This method accounts for the contamination of photons from neighboring sky regions into each detector (sub-)region due to the relatively broad point spread function (PSF) of the X-ray Mirror Assembly (XMA). We include the PSF scattering effects into our model following the multi-source ARF technique described in Hitomi Collaboration et al. (2018), using the Chandra image in the 0.5–7.0 keV band as the input.

We divided the cluster core into five sky regions, labeled A through E as shown in figure 1 overlaid on the Chandra image of the cluster. The regions are selected to focus on interesting parts of the core — for example, Reg-A isolates the ICM inside the prominent cold front. We then selected regions in the Resolve field of view that follow these sky regions as closely as possible, and extracted spectra from those regions. To account for mixing between the sky and detector regions, we used the high-resolution Chandra image as a model of the X-ray surface brightness to compute the contribution of each sky region to individual detector regions. We performed a simultaneous fit of all spectra and model components corresponding to the individual sky regions. To incorporate photons scattered from outside the field of view into the spectral model, the boundaries of the sky regions were extended beyond the detector field of view. Specifically, regions A, B, and D were extended to reach the cold front boundaries identified by Ichinohe et al. (2021), while regions C and E were defined as circular regions with radii of 3 arcmin, centered on the P2 pointing position. We note that the leak-in contributions from outside the cold front boundaries are estimated to be approximately 4% for Reg-A, 2% for Reg-B, and much less for other regions. Since the parameters in these outer region cannot be reliably constrained with the current data, we simply ignored it and did not include it in the spectral modeling.

On the detector side, spectra were extracted independently for each observation. As shown in figure 1, for the P1 pointing, we divided the field of view into regions a, b, and d, while for the P2 pointing, we used regions b', c', d', and e', resulting in seven detector regions in total. Since each detector region may receive photon contributions from all five sky regions, we generated a cross-region ARF for every combination of sky and detector regions. By this approach, we can construct a self-consistent spectral model that reflects the instrument's spatial resolution and accurately models spatial photon mixing. Regions are selected to be wide enough in comparison with the PSF (which has a 1.3 arcmin half-power diameter) so that in each spectrum the dominant fraction of the photons originates in the underlying sky region.

Each spectrum was simultaneously fitted using five *bapec* models corresponding to regions A–E, with individual components convolved with their respective ARFs. The physical parameters — such as temperature, metal abundance, redshift, velocity dispersion and normalization — were tied across all spectra to which the same sky region contributed. Figure 3 shows the two examples of spectra in detector regions, plotted together with fitted contributions from the five sky regions. As expected, Reg-A component is dominant in Det-a region, and Red-D component is dominant in Det-(d+d') region.

The fitted results are presented in figure 4. For reference, the

fitting results without accounting for SSM in each detector region are summarized in table 2 in the Appendix. We note that, although our sky regions extend beyond the boundaries of the detector as described above, the derived ICM parameters are most relevant for the parts of the regions that are inside the field of view, where we have the data. If there are parameter variations within each sky region, we would not be able to detect it without additional Resolve coverage.

Regions A and D, located near the cold front, exhibit bulk velocities consistent with that of the BCG, $+14^{+124}_{-105}$ km s^{−1} and $−25^{+37}_{-37}$ km s^{−1}, respectively. In contrast, Reg-B, located south-east of the BCG, exhibits a significant blueshift, $−228^{+24}_{-30}$ km s^{−1}. Meanwhile, the northern side of the BCG shows a redshift relative to the BCG: the Reg-C exhibits a bulk velocity of 66^{+44}_{-39} km s^{−1}, and the Reg-E shows 93^{+44}_{-35} km s^{−1}. The velocity difference between Reg-B and Reg-E thus amounts to approximately 300 km s^{−1}. The bulk velocities of these regions differ by more than 4σ .

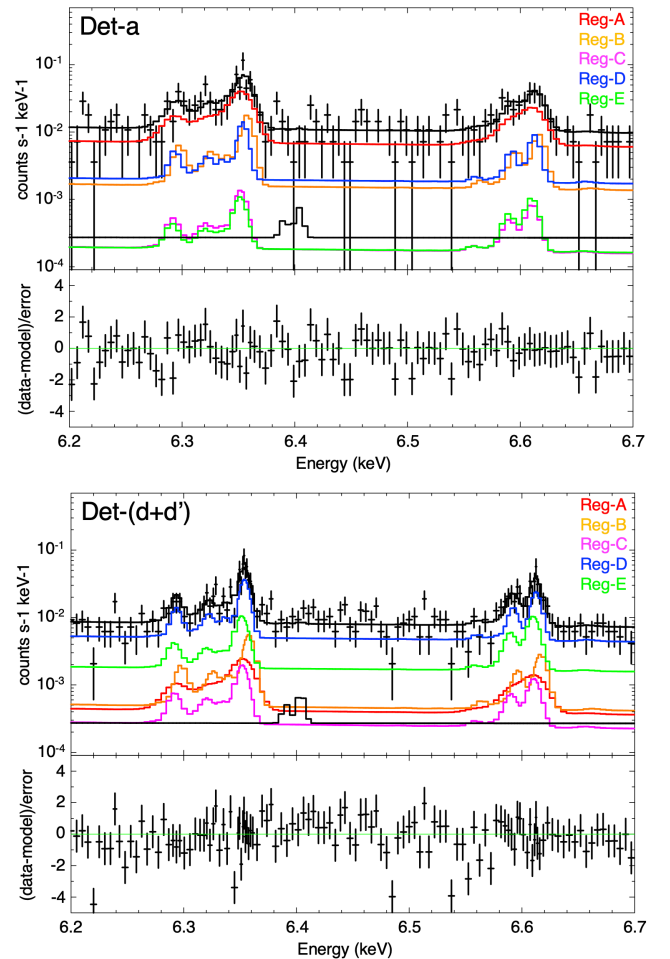


Fig. 3. Resolved spectra around the Fe K α lines of Det-a (upper) and Det-d+d' (lower) for the SSM analysis. The spectra of regions d and d' are co-added using *mathpha* for display purposes. The solid lines represent the modeled contributions from individual regions: Reg-A (red), Reg-B (orange), Reg-C (magenta), Reg-D (blue), and Reg-E (green). Alt text: Two line graphs. In the two panels, the x axis shows the energy from 6.2 to 6.7 kilo electron volt. The y axis shows the count from 0.0009 to 0.7 counts per second and per kilo electron volt, and the residuals of minus 5 to 5 in lower part.

The velocity dispersion across the field generally lies in the range of 100–200 km s^{−1}, comparable to that of the Coma cluster. An enhancement is observed near the south end of the cold front: Reg-A shows a velocity dispersion of 405_{-96}^{+191} km s^{−1}. The spectrum of Det-a around the Fe K α lines is shown in the upper panel of figure 3. The difference in the line width between the high-dispersion Det-a and the low-dispersion Det-d spectra is clearly visible. Notably, Reg-A is the highest velocity dispersions reported by XRISM for the several clusters observed to date. For comparison, previous studies have reported typical values of ~ 100 –200 km s^{−1} in the central regions of nearby clusters such as Perseus, Abell 2029, and Coma (e.g., Hitomi Collaboration et al. 2016; XRISM Collaboration et al. 2025a; XRISM Collaboration et al. 2025b).

The temperature map reveals that the ICM is relatively hot across most regions. The central regions and the southeastern regions are slightly cooler, around 7.6–7.7 keV. In contrast, the Reg-E exhibits higher temperatures of $11.0_{-1.0}^{+1.1}$ keV, consistent with previous Chandra and XMM-Newton observations that identified a high-temperature belt structure (Govoni et al. 2004; Ichinohe et al. 2021). The abundance map shows modest spatial variations, ranging from 0.28 to 0.46 solar. Higher abundances (~ 0.45 solar) are found in regions B and E, near the BCG, while somewhat lower values (0.28–0.38 solar) are observed in regions A and D.

We also performed narrow-band SSM fits restricting within 6.2–6.7 keV range, where the temperature is primarily constrained by the Fe–K line ratio. The best-fit values from these fits are shown in parentheses in figure 3, and are consistent with those from the broadband fits.

4 Discussion

The mean redshifts in the two XRISM/Resolve pointings covering the core of the A2319 cluster are consistent with the BCG optical redshift within 40 km s^{−1}. Our spatially resolved velocity measurements uncover two significant features in this sloshing core — (a) a ~ 300 km s^{−1} variation in the line of sight velocities across the core, with one region (Reg-B in figure 4) showing a highly significant >200 km s^{−1} deviation from the mean, while other regions showing velocities within 100 km s^{−1} of the mean, and (b) a relatively high line of sight velocity dispersion (~ 400 km s^{−1}) in Reg-A immediately inside the cold front, while its line of sight velocity is close to the mean.

4.1 Sloshing inclined to the skyplane

If the low-entropy gas is rotating as a result of sloshing, the central ICM with the lowest entropy and the ICM near the cold front should be moving in three-dimensional space. Hydrodynamical simulations of minor mergers (ZuHone et al. 2016) between clusters demonstrated that, when the sloshing plane is oriented along the line of sight, a velocity difference amounts to $M=0.2$ –0.3. Low-entropy ICM in A2319 has a temperature of ~ 8.5 keV and its sound speed is estimated to be $C_s = (\gamma k_B T / \mu m_p)^{1/2} = 1500$ km s^{−1}, assuming a mean molecular weight $\mu = 0.6$ and an adiabatic index $\gamma = 5/3$. In this case, a velocity difference of 300–450 km s^{−1} would be expected.

Chandra X-ray image shows a “spiral structure” associated with sloshing motions, extending counterclockwise from the BCG to the east and then to the south, spanning approximately 200 kpc (see figure 8 of Ichinohe et al. 2021). It indicates that the sloshing motion has some motion in the skyplane. Significant blue-shifted

motion at Reg B (around the east edge of the cold front) and almost zero red shift in Reg-A (to the south) suggest an ICM flow following the BCG is rotating with some inclination to the line of sight, and the component in Reg-B is “falling” into the BCG potential from the far side. The Chandra X-ray brightness and temperature maps show that Reg-B is likely a distinct structure in the sloshing core, with the lowest specific entropy (Ichinohe et al. 2021). In simulations of sloshing (e.g., Ascasibar & Markevitch 2006), the lowest-entropy gas is continuously separating itself from the rest of the moving core, falling towards the peak of the gravitational potential, overshooting it, and repeating the process, and our velocity findings appear consistent with this picture. Although the detailed geometry of the ICM flow is not clear, the “spiral structure” and the “falling low entropy gas” suggest that the sloshing, or ICM rotation in the central region, has some inclination to the skyplane.

4.2 Development of turbulence near the cold front

The velocity dispersion map in figure 4 shows that the ICM near the southern part of the cold front (Reg-A) has a velocity dispersion value of 405_{-96}^{+191} km s^{−1}, which may reflect enhanced turbulence or projection effects in the downstream of the sloshing flow. In observations of large-scale rotational motions such as sloshing, emission lines can be broadened due to the superposition of multiple ICM components with different line-of-sight velocities (Inogamov & Sunyaev 2003). We cannot distinguish based on our data alone whether it is turbulence or shear; however, the Chandra image strongly suggests that the front at this location is oriented in the sky plane, with the velocity flows occurring in the sky plane, thus strong shear along the line of sight is less likely than turbulence. Of course, there can be two or more overlaid components with different line of sight velocities there, as discussed later.

If we interpret the line broadening as isotropic turbulence, then its turbulent Mach number near the cold front reaches $M_{3D} = 0.49_{-0.12}^{+0.23}$, indicating relatively stronger subsonic turbulence. It corresponds to a nonthermal pressure (NT) fraction of

$$\frac{P_{NT}}{P_{tot}} = \frac{M_{3D}^2}{M_{3D}^2 + 3/\gamma} = 11.2_{-4.7}^{+10.6}\%, \quad (1)$$

assuming an adiabatic index of $\gamma = 5/3$ (e.g., Eckert et al. 2019). This may reflect continuous energy injection by sloshing-induced shear flows, or possibly an evolution from initially anisotropic motions toward a more isotropic turbulent state over time, as discussed in the context of the Coma cluster (e.g., Zhuravleva et al. 2019; Churazov et al. 2012).

Such high velocity dispersion near the cold front may also be associated with eddy-like features produced by shear-induced instabilities. Previous studies based on Chandra images have suggested the presence of Kelvin Helmholtz instability (KHI) along the cold front boundary in A2319, especially to the west of the segment of the front in Reg-A, as indicated by image residual and temperature structures (Ichinohe et al. 2021). If such KHI-induced eddies are present, they could introduce anisotropic velocity perturbations that are observed as enhanced dispersion when spatially averaged by the PSF of XMA. Such eddies would also drive turbulence. This scenario is consistent with the observed broadening, the variations of the line of sight velocity within Reg-A, and the possible redistribution of kinetic energy into turbulence in the downstream region.

Alternatively, part of the observed velocity dispersion may result from bulk flow components projected along the line of sight. We divided Det-a into two sub-regions, east and west, but could

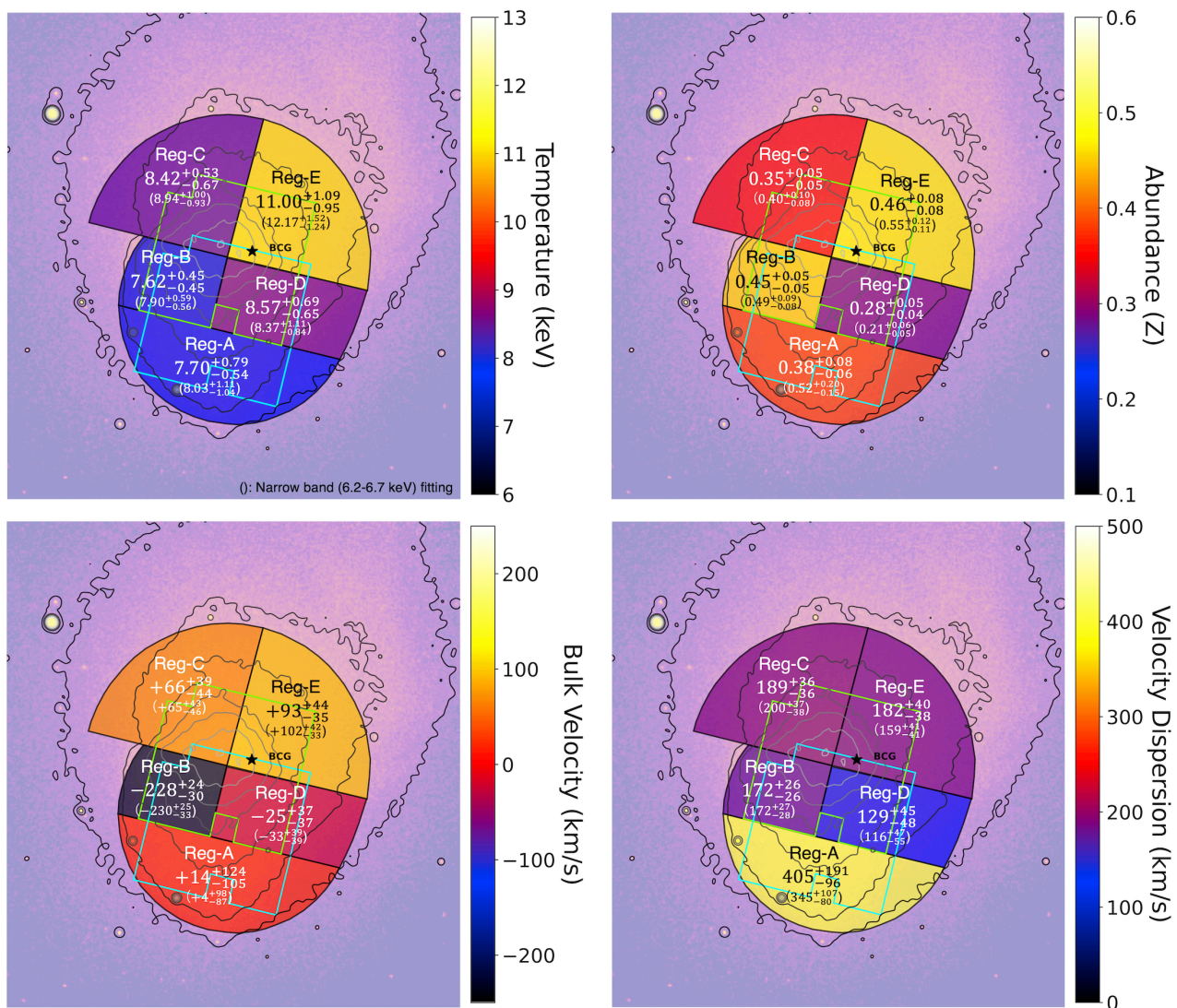


Fig. 4. Maps of temperature (top left), abundance (top right), bulk velocity (bottom left), and velocity dispersion (bottom right), based on the spatial regions defined in figure 1. All maps are derived from broad-band fits in the 3.0–9.5 keV range; values in parentheses indicate the corresponding results from the narrow-band fits (6.2–6.7 keV). The black star indicates the position of the BCG. Contours represent the X-ray surface brightness, highlighting the correspondence with spatial structures. The boxes indicate the fields of view corresponding to observations P1 (cyan) and P2 (green). The units of the color bars are, in order: keV, solar, km s⁻¹, and km s⁻¹. Alt text: Four color maps arranged in two rows and two columns, each with right ascension on the horizontal axis and declination on the vertical axis. The upper left map shows temperature in kilo-electronvolts ranging from 6.0 to 13.0. The upper right map shows abundance in solar units ranging from 0.1 to 0.6. The lower left map shows bulk velocity in kilometers per second ranging from minus 250 to plus 250. The lower right map shows velocity dispersion in kilometers per second ranging from 0 to 500.

not find statistically significant velocity difference. Therefore, overall structure of the possible bulk motion is not clear. In the downstream of the sloshing flow, the ICM may be diffusing perpendicularly to the flow direction—that is, along our line of sight—leading to line broadening due to superposed velocity components. In either case, the kinetic energy of the flow would be redistributed into turbulence and lateral motions, potentially causing a decrease in the flow velocity downstream. Indeed, a slight drop in the line-of-sight velocity is observed in the southeastern region, supporting the presence of such redistribution. Another possibility is the line of sight velocities diverging in the opposite directions at the nose of the front, as seen in simulations at certain stages and locations (e.g., Ascasibar & Markevitch 2006), but this is unlikely at the current stage, with the spiral structure that we clearly see in the image, where most of the flow velocity inside the front should be in the

sky plane along the front.

4.3 High redshift clump (A2319B)

As stated in the introduction, A2319 hosts an isolated optical galaxy group (A2319B) located approximately 10 arcminutes northwest of the center, with an average velocity of 18636 km s⁻¹ or $z = 0.06212$ (Oegerle et al. 1995), redshifted by 3000 km s⁻¹ from the BCG. Identifying ICM emission from A2319B is important to understand the merger geometry around this cluster. Markevitch (1996) used ASCA data and found that the region located at A2319B is relatively cooler compared to the surrounding areas. Using Suzaku XIS data, Sugawara et al. (2009) further discovered that this cold region has a higher elemental abundance compared to the surrounding regions. On the other hand, red-

shift measurements showed no significant signs of redshifted ICM compared to the surrounding areas. This non-detection is likely attributable to the limited energy resolution of the CCD detectors, which makes it challenging to resolve redshift differences of a few thousand km s^{-1} amidst line blending and calibration uncertainties.

Although the Resolve field of view does not cover that region, the galaxies from that subcluster do spread across the whole cluster, and we searched for an ICM component redshifted by 3000 km s^{-1} using data from Resolve, which offers more than 30 times higher energy resolution than XIS. We added a model component with a velocity of 18636 km s^{-1} to the baseline model listed in table 1 and performed spectral fitting. The velocity dispersions were fixed to the values given in table 1. In the lower panel of figure 2, the expected line centers of He-like Fe $K\alpha$ complex (w, x, y, z) and H-like Fe $\text{Ly}\alpha_{1,2}$ are indicated by blue lines. In the fitting results, the upper limit of the flux corresponding to the component at 18636 km s^{-1} was calculated to be $2.66 \times 10^{-16} \text{ erg s}^{-1} \text{ cm}^{-2} \text{ sr}^{-1}$ (0.5–10.0 keV) at a 90% confidence interval. This value can be considered as statistical fluctuations, and it can be concluded that the component at 18636 km s^{-1} was not detected in this observation.

4.4 High temperature ICM in northern region

The temperature map in figure 4 shows that Reg-E has an average temperature of approximately 11 keV, which is higher than that of the surrounding regions. Chandra data (Ichinohe et al. 2021) also show that Reg-E includes another cold front, distinct from the main one on the eastern side of the core. This secondary front is located at a much smaller off-center distance and exhibits a significant temperature gradient. It is a site where hot gas from larger radii is driven inward by sloshing motions, approaching the cluster center and eventually mixing with the cooling core gas. This process provides a heat influx into the core and may counteract runaway cooling (Fujita et al. 2004; ZuHone et al. 2010).

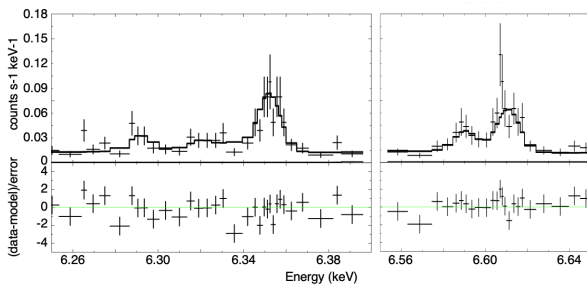


Fig. 5. Zoom-in of the Resolve spectrum around the He-like (left) and H-like (right) Fe lines of the Det-e'. Data are binned by a factor of 2 eV for display. Alt Text: Two line graphs. In the left panel, the x axis shows the energy from 6.25 to 6.40 kilo electron volt. In the lower right panel, the x axis shows the energy from 6.55 to 6.65 kilo electron volt. The y axis shows the count from 0.0 to 0.18 counts per second and per kilo electron volt, and the residuals of minus 5 to 5 in lower part.

It is interesting to try to detect any velocity differences within this region, given that it includes gas inside and outside the cold front, which has different temperatures (with the cooler, denser gas located inside the cold front). Reg-E is redshifted by about 90 km s^{-1} relative to the BCG. The spectrum of Det-e' (see figure 5) shows that the position of the He-like Fe lines (6.2–6.4 keV), which come from gas in a broad range of temperatures, matches

well between the model and the data, while that of the H-like Fe lines (6.5–6.7 keV), which originate from hotter gas phases, is more redshifted in the data. When fitting the spectrum with the temperature fixed, the bulk velocity relative to the BCG is found to be $37.7^{+39.7}_{-38.6} \text{ km s}^{-1}$ (6.2–6.4 keV) and $92.6^{+40.1}_{-33.5} \text{ km s}^{-1}$ (6.5–6.7 keV), respectively. The difference suggests that the low-temperature and high-temperature ICM components have different velocities and these components are mixed in the spectrum. The current dataset, however, lacks sufficient statistical significance to clearly separate these two spectral components. Additional XRISM pointing(s) around the high-entropy ICM region will solve this in the future.

5 Conclusions

We presented results from the XRISM observations of the core of A2319, one of the X-ray brightest nearby hot clusters, focusing on its kinematic structure. The ICM temperature was found to be approximately 8 keV across the cluster core, with a prominent cold front structure and a region of elevated temperature (~ 10 keV) in the northwest. The bulk velocity around the BCG is consistent with that of the BCG within 40 km s^{-1} . A blueshift of up to $\sim 230 \text{ km s}^{-1}$ is observed along the eastern edge of the cold front, located southeast of the BCG, where the gas with the lowest specific entropy is found, while the region farther south along the cold front shows only a modest redshift. However, in the southern region inside that front, the velocity dispersion increases to $\sim 400 \text{ km s}^{-1}$, suggesting the development of turbulence. These features indicate that the ICM is undergoing sloshing motion with a certain inclination angle relative to the plane of the sky, following the motion of the BCG. We also investigated the possible presence of high-redshift ICM associated with the subcluster A2319B but found no significant detection within the current field of view.

Overall, these results provide new insights into the internal dynamics of A2319, highlighting sloshing motions that occur with a moderate inclination to the plane of the sky. The gas phases with different specific entropies move independently of each other, as expected from simulations of sloshing. They also contribute to our understanding of the cluster's three-dimensional geometry and the role of turbulence in shaping the thermal and kinematic structure of the ICM. Deeper observations and additional pointings will be essential to further explore the detailed nature of the high-temperature gas and the turbulent properties of the sloshing flow.

Acknowledgments

We gratefully acknowledge the hard work over many years of all of the engineers and scientists who made the XRISM mission possible. Part of this work was performed under the auspices of the U.S. This work was supported by the JSPS Core-to-Core Program, JPJSCCA20220002. The material is based on work supported by the Strategic Research Center of Saitama University. Department of Energy by Lawrence Livermore National Laboratory under Contract DE-AC52-07NA27344. The material is based upon work supported by NASA under award numbers 80GSFC21M0002 and 80GSFC24M0006. This work was supported by JSPS KAKENHI grant numbers JP19K14762, JP19K21884, JP20H00157, JP20H01946, JP20H01947, JP20H05857, JP20K04009, JP20K14491, JP20KK0071, JP21H01095, JP21H04493, JP21K03615, JP21K13958, JP21K13963, JP22H00158,

JP22H01268, JP22K03624, JP23H00121, JP23H00151, JP23H01211, JP23H04899, JP23K03454, JP23K03459, JP23K13154, JP23K20239, JP23K20850, JP23K22548, JP24H00253, JP24K00638, JP24K00672, JP24K00677, JP24K17093, JP24K17104, and JP24K17105. This work was supported by NASA grant numbers 80NSSC22K1922, 80NSSC18K0978, 80NSSC18K0988, 80NSSC18K1684, 80NSSC20K0733, 80NSSC20K0737, 80NSSC20K0883, 80NSSC23K0650, 80NSSC23K1656, 80NSSC24K0678, 80NSSC24K1148, 80NSSC24K1774. LC acknowledges support from NSF award 2205918. CD acknowledges support from STFC through grant ST/T000244/1. LG acknowledges financial support from Canadian Space Agency grant 18XARMSTMA. NO acknowledges partial support by the Organization for the Promotion of Gender Equality at Nara Women's University. MS acknowledges the support by the RIKEN Pioneer Project Evolution of Matter in the Universe (r-EMU) and Rikkyo University Special Fund for Research (Rikkyo SFR). AT and the present research are in part supported by the Kagoshima University postdoctoral research program (KU-DREAM). SY acknowledges support by the RIKEN SPDR Program. TY acknowledges support by NASA under award number 80GSFC24M0006. IZ acknowledges partial support from the Alfred P. Sloan Foundation through the Sloan Research Fellowship. SE acknowledges the financial contribution from the contracts Prin-MUR 2022 supported by Next Generation EU (M4.C2.1.1, n.20227RNLY3 The concordance cosmological model: stress-tests with galaxy clusters), ASI-INAF Athena 2019-27-HH.0, "Attività di Studio per la comunità scientifica di Astrofisica delle Alte Energie e Fisica Astroparticellare" (Accordo Attuativo ASI-INAF n. 2017-14-H.0), and from the European Union's Horizon 2020 Programme under the AHEAD2020 project (grant agreement n. 871158). LL acknowledges the financial contribution from the INAF grant 1.05.12.04.01. YO would like to take this opportunity to thank the "Nagoya University Interdisciplinary Frontier Fellowship" supported by Nagoya University and JST, the establishment of university fellowships towards the creation of science technology innovation, Grant Number JPMJFS2120. Y.O. was supported by the Sasakawa Scientific Research Grant from The Japan Science Society.

Appendix 1 Energy scale calibration and uncertainty

The gain of the XRISM Resolve microcalorimeter detectors is affected by its environment including the temperature of the 50 mK heat sink, bolometric effects of the detectors themselves due to thermal radiation from the instrument thermal shields, and the temperature of the amplifier and bias electronics in the warm instrument electronics. The net effect is a detector gain, and thus energy scale error, that is time dependent. XRISM carries multiple on-board calibration sources to monitor the time dependent gain and to reconstruct the time dependent energy scale using a non-linear correction method described in Porter et al. (2016).

Current XRISM observations obtain gain fiducials by rotating ^{55}Fe x-ray sources on the Resolve filter wheel into the instrument field of view for 30 minute intervals strategically placed during each observation. The gain correction scheme, described in Porter 2025 and Sawada 2025, is highly effective in reconstructing the energy scale, typically to within 0.1–0.2 eV at 6 keV. The gain fiducial intervals are closely spaced around events that disturb the gain

which include recycling of the 50 mK refrigerator and large scale temperature changes of the instrument electronics due to changes in the spacecraft orientation after slewing to a new target. Outside of these large disturbances, the time dependent instrument gain is extremely linear and is only sparsely sampled with gain fiducials approximately every 20 hours in the standard XRISM/Resolve observing strategy. Finally, the Resolve instrument includes a calibration pixel that is part of the microcalorimeter array but located just outside the field of view. The calibration pixel is continuously illuminated by a heavily collimated ^{55}Fe x-ray source. In standard XRISM/Resolve observations, the calibration pixel is used to measure the efficacy of the energy scale reconstruction by comparing the Mn Ka fiducial line offset and resolution during the observation, but only gain corrected using the sparsely sampled fiducial intervals used for the main observation. These metrics are a standard product of the XRISM pipeline.

As the observations of A2319 were carried out very early in the XRISM commissioning phase, before the modern observing strategy was implemented, the standard, sparsely sampled gain fiducial methodology was not employed. However, during this time, the Resolve instrument team was benchmarking the on-orbit instrument performance using the same ^{55}Fe filter wheel sources now used for gain reconstruction. An event history plot for the A2319 "core" observations is shown in figure 6. During the A2319 observations, there are long periods with and without the filter wheel ^{55}Fe sources in the field of view. While the periods with the ^{55}Fe sources are not usable for science, they provide adequate gain calibration fiducials for the periods without the sources in the field of view. This required some careful handling of the observation data because there were subtleties that are not properly handled by the standard Resolve pipeline gain calibration methodology. For example, the beginning fiducial for OBSID 000101000 actually occurs during the previous OBSID, similarly for OBSIDs 000102000 and 000103000. There is also a small 50 mK set point error in the 50 mK temperature controller during OBSID 000101000 that was corrected by cross-calibration with the cal pixel (the set point error occasionally occurred during passages through the South Atlantic Anomaly and was permanently fixed later in commissioning). During OBSID 000103000 there was a recycle event of the Adiabatic Demagnetization Refrigerator (ADR) that cools the 50 mK detector heat sink. This heavily disturbs the detector gain. In this case, the detector gain was forward extrapolated from the earlier fiducial interval up to the ADR recycle since this is firmly within the linear gain drift period for the detectors. The period after the ADR recycle was back-extrapolated from the following gain fiducial, but only during the linear portion of the gain history which begins 6 hours after the ADR recycle (Porter 2025). Finally, the last portion of OBSID 000103000 has no ending fiducial measurement, but is firmly within the linear gain drift period, and was thus forward extrapolated from the prior fiducial region.

In all cases, the calibration pixel was analyzed using the same time-dependent gain correction method described above for the main array. However, the calibration pixel is continuously illuminated, so we fit the Mn Ka line from the ^{55}Fe source to track the energy resolution and the line shift as a measure of the efficacy of the energy scale reconstruction. This is the same methodology used in all Resolve observations. This gave cal pixel resolutions of 4.45 ± 0.02 , 4.45 ± 0.02 , and 4.46 ± 0.02 eV FWHM at 5.9 keV for OBSIDs 000102000, 000102000, and 000103000 respectively, which is exactly inline with the ensemble of XRISM/Resolve observations (Porter 2025; Kelley 2025; Leutenegger 2025). Similarly, the energy scale errors were

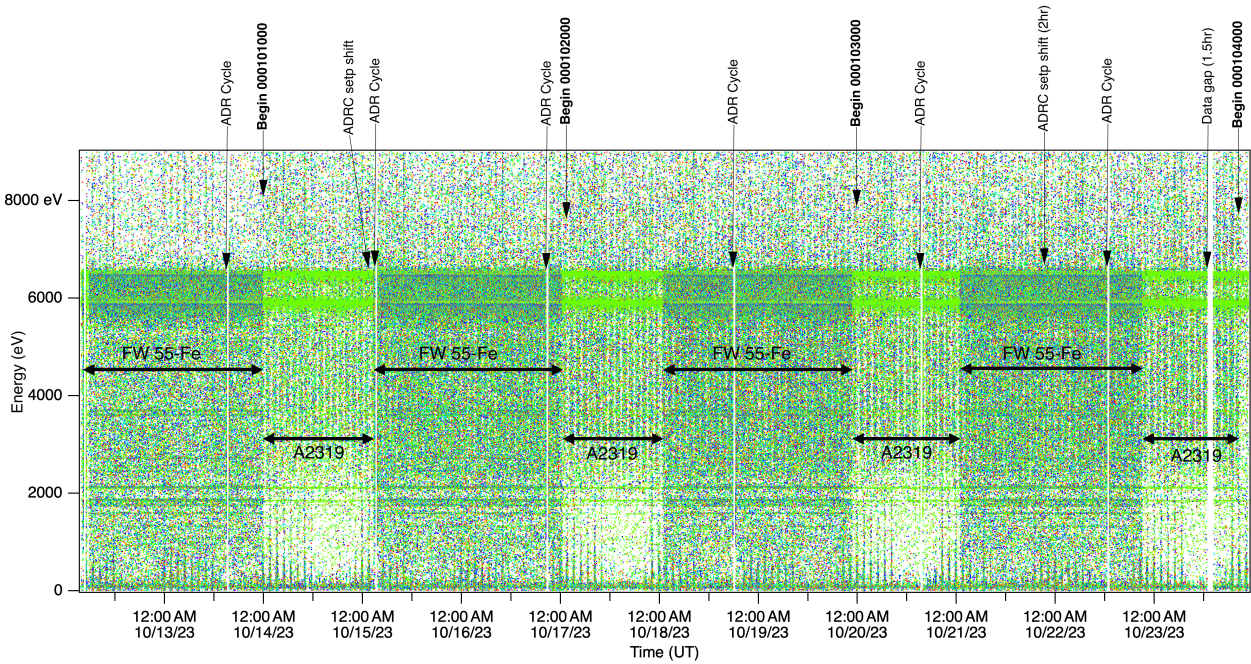


Fig. 6. An overview of the A2319 observations where each “dot” represents an x-ray event color coded by pixel. The start of each OBSID is indicated along with the positions of the ADR refrigerator recycles. Further, the periods when the filter wheel ^{55}Fe x-ray sources were in the field of view are indicated along with the unobscured observations of Abel 2319. The light green points at 5.9 and 6.4 keV are the continuously illuminated calibration pixel. Alt text: Two-dimensional scatter plot of Resolve photon events. In the panel, x-axis is time, from 12 to 24 October 2023, and y-axis is photon energy after gain calibration, from 0 eV to 9000 eV. There are four periods with ^{56}Fe irradiation and another four without. The latter can be used for our analyses.

-0.41 ± 0.01 , 0.14 ± 0.01 , and 0.04 ± 0.01 eV for the same OBSIDs. Using the standard resolve method for estimating the energy scale systematic uncertainties (Eckart 2025), we add the cal pixel uncertainties in quadrature with estimates of the underlying energy scale uncertainty of 0.3 eV in the band 5.4–9 keV, and 1 eV outside of that band. This yields energy scale uncertainties for these observations of 0.51, 0.33, and 0.30 eV in the energy band of 5.4–9 keV, respectively.

Because these A2319 observations need special care on gain handling, we present the ICM parameter maps before applying the SSM correction in table 2. As expected, tendencies of the parameters are very similar to those of figure 4. SSM corrects the smearing effect caused by the modest PSF of XRISM, and therefore differences between the parameters are enhanced after correction.

References

- Arnaud, K. A. 1996, in *Astronomical Society of the Pacific Conference Series*, Vol. 101, *Astronomical Data Analysis Software and Systems V*, ed. G. H. Jacoby & J. Barnes, 17
- Ascasibar, Y. & Markevitch, M. 2006, *ApJ*, 650, 102
- Botteon, A., Gastaldello, F., & Brunetti, G. 2018, *MNRAS*, 476, 5591
- Brunetti, G. & Jones, T. W. 2014, *International Journal of Modern Physics D*, 23, 1430007
- Cash, W. 1979, *ApJ*, 228, 939
- Chadayammuri, U., Zuhone, J., Nulsen, P., et al. 2022, *MNRAS*, 509, 1201
- Churazov, E., Vikhlinin, A., Zhuravleva, I., et al. 2012, *MNRAS*, 421, 1123
- Eckart. 2025, manuscript submitted to JATIS
- Eckert, D., Ghirardini, V., Ettori, S., et al. 2019, *A&A*, 621, A40
- Farnsworth, D., Rudnick, L., Brown, S., & Brunetti, G. 2013, *ApJ*, 779, 189
- Feretti, L., Giovannini, G., & Böhringer, H. 1997, *New Astronomy*, 2, 501
- Feretti, L., Giovannini, G., Govoni, F., & Murgia, M. 2012, *A&AR*, 20, 54
- Fujita, Y., Matsumoto, T., & Wada, K. 2004, *ApJL*, 612, L9
- Ghirardini, V., Ettori, S., Eckert, D., et al. 2018, *A&A*, 614, A7
- Govoni, F., Enßlin, T. A., Feretti, L., & Giovannini, G. 2001, *A&A*, 369, 441
- Govoni, F., Markevitch, M., Vikhlinin, A., et al. 2004, *ApJ*, 605, 695
- Heinrich, A., Zhuravleva, I., Zhang, C., et al. 2024, *MNRAS*, 528, 7274
- Hitomi Collaboration, Aharonian, F., Akamatsu, H., et al. 2016, *Nature*, 535, 117
- Hitomi Collaboration, Aharonian, F., Akamatsu, H., et al. 2018, *PASJ*, 70, 9
- Hurier, G., Adam, R., & Keshet, U. 2019, *A&A*, 622, A136
- Ichinohe, Y., Simionescu, A., Werner, N., Markevitch, M., & Wang, Q. H. S. 2021, *MNRAS*, 504, 2800
- Inogamov, N. A. & Sunyaev, R. A. 2003, *Astronomy Letters*, 29, 791
- Kelley. 2025, manuscript submitted to JATIS
- Kluge, M. & Bender, R. 2023, *ApJS*, 267, 41
- Kravtsov, A. V. & Borgani, S. 2012, *ARA&A*, 50, 353
- Leutenegger. 2025, manuscript submitted to JATIS
- Li, M., McNamara, B. R., & Zhuravleva, I. 2025, *MNRAS*, 537, 2198
- Lodders, K., Palme, H., & Gail, H. P. 2009, *Landolt BÖmstein*, 4B, 712
- Markevitch, M. 1996, *ApJL*, 465, L1
- Markevitch, M. & Vikhlinin, A. 2007, *Phys. Rep.*, 443, 1
- Million, E. T. & Allen, S. W. 2009, *MNRAS*, 399, 1307
- Mohapatra, R. & Sharma, P. 2019, *MNRAS*, 484, 4881
- Molendi, S., De Grandi, S., Fusco-Femiano, R., et al. 1999, *ApJL*, 525, L73
- Oegerle, W. R., Hill, J. M., & Fitchett, M. J. 1995, *AJ*, 110, 32
- Okabe, N. & Umetsu, K. 2008, *PASJ*, 60, 345
- Omiya, Y., Nakazawa, K., Matsushita, K., et al. 2023, *PASJ*, 75, 37
- Omiya, Y., Nakazawa, K., Tamura, T., et al. 2024, *A&A*, 689, A173
- Owers, M. S., Randall, S. W., Nulsen, P. E. J., et al. 2011, *ApJ*, 728, 27
- Paul, S., Iapichino, L., Miniati, F., Bagchi, J., & Mannheim, K. 2011, *ApJ*, 726, 17
- Porter, F. S. 2025, manuscript submitted to JATIS
- Porter, F. S., Chiao, M. P., Eckart, M. E., et al. 2016, *Journal of Low Temperature Physics*, 184, 498
- Ricker, P. M. & Sarazin, C. L. 2001, *ApJ*, 561, 621
- Sanders, J. S., Dennerl, K., Russell, H. R., et al. 2020, *A&A*, 633, A42

Table 2. Best-fit Parameters of the detector regions in 3.0–9.5 keV energy range.

Parameters	Det-a*	Det-b	Det-d	Det-b'	Det-c'	Det-d'	Det-e'
kT (keV)	$7.66^{+0.35}_{-0.37}$	$7.72^{+0.49}_{-0.49}$	$8.66^{+0.69}_{-0.69}$	$8.42^{+0.42}_{-0.35}$	$8.50^{+0.32}_{-0.34}$	$9.26^{+0.45}_{-0.40}$	$9.84^{+0.49}_{-0.48}$
Abundance (Z_{\odot})	$0.35^{+0.04}_{-0.04}$	$0.39^{+0.05}_{-0.05}$	$0.34^{+0.05}_{-0.05}$	$0.39^{+0.04}_{-0.03}$	$0.37^{+0.03}_{-0.03}$	$0.36^{+0.04}_{-0.04}$	$0.40^{+0.04}_{-0.04}$
Redshift ($\times 10^{-2}$)	$5.4435^{+0.01852}_{-0.01821}$	$5.4367^{+0.01351}_{-0.01321}$	$5.4667^{+0.01302}_{-0.0106}$	$5.4155^{+0.01116}_{-0.0102}$	$5.4689^{+0.0084}_{-0.0093}$	$5.4468^{+0.0105}_{-0.0112}$	$5.4817^{+0.01000}_{-0.0082}$
Relative Velocity (km s $^{-1}$)	$-60.0^{+55.6}_{-54.6}$	$-76.3^{+40.5}_{-39.6}$	$+13.8^{+39.0}_{-31.6}$	$-140.0^{+33.5}_{-30.6}$	$+20.1^{+25.2}_{-28.0}$	$-46.0^{+31.4}_{-33.7}$	$+58.6^{+30.0}_{-24.5}$
Velocity dispersion (km s $^{-1}$)	312^{+54}_{-44}	232^{+32}_{-31}	147^{+37}_{-40}	246^{+36}_{-32}	206^{+24}_{-23}	195^{+41}_{-38}	193^{+28}_{-26}
C-stat/d.o.f	7652/12994	9748/12994	9103/12994	20243/25992	20675/25992	19058/25992	20627/25992

* Spectral fitting results obtained without applying SSM. Det-a, b and d are in the data of OBSID:000101000, almost matching with Reg-A, B, and D. Det-b', c', d' and e' are in the data of OBSID:000102000 and 000103000, almost matching Reg-B, C, D and E.

Sawada. 2025, manuscript submitted to JATIS

Shi, X., Nagai, D., Aung, H., & Wetzel, A. 2020, MNRAS, 495, 784

Smith, R. K., Brickhouse, N. S., Liedahl, D. A., & Raymond, J. C. 2001, ApJL, 556, L91

Storm, E., Jeltama, T. E., & Rudnick, L. 2015, MNRAS, 448, 2495

Sugawara, C., Takizawa, M., & Nakazawa, K. 2009, PASJ, 61, 1293

Tashiro, M., Maejima, H., Toda, K., et al. 2020, in Society of Photo-Optical Instrumentation Engineers (SPIE) Conference Series, Vol. 11444, Space Telescopes and Instrumentation 2020: Ultraviolet to Gamma Ray, ed. J.-W. A. den Herder, S. Nikzad, & K. Nakazawa, 1144422

Uchida, H., Mori, K., Tomida, H., et al. 2025, arXiv e-prints, arXiv:2503.20180

Ueda, S. & Ichinohe, Y. 2024, ApJ, 973, 98

van Weeren, R. J., de Gasperin, F., Akamatsu, H., et al. 2019, Space Sci. Rev., 215, 16

Voit, G. M. 2005, Reviews of Modern Physics, 77, 207

Walker, S. A., Sanders, J. S., & Fabian, A. C. 2016, MNRAS, 461, 684

Wang, Q. H. S. 2019, Phd thesis, University of Maryland, College Park, MD

Willingale, R., Starling, R. L. C., Beardmore, A. P., Tanvir, N. R., & O'Brien, P. T. 2013, MNRAS, 431, 394

XRISM Collaboration, Audard, M., Awaki, H., et al. 2025a, ApJL, 982, L5

XRISM Collaboration, Audard, M., Awaki, H., et al. 2025b, ApJL, 985, L20

Yuan, Z. S. & Han, J. L. 2020, MNRAS, 497, 5485

Zhuravleva, I., Allen, S. W., Mantz, A., & Werner, N. 2018, ApJ, 865, 53

Zhuravleva, I., Churazov, E., Schekochihin, A. A., et al. 2019, Nature Astronomy, 3, 832

ZuHone, J. A., Markevitch, M., & Johnson, R. E. 2010, ApJ, 717, 908

ZuHone, J. A., Miller, E. D., Simionescu, A., & Bautz, M. W. 2016, ApJ, 821, 6